

# Supplementary Information

## Submicron Resolution Hyperspectral Quantum Rod Thermal Imaging of Microelectronic Devices

*Bahar Öner\**, *James W. Pomeroy* and *Martin Kuball\**

Center for Device Thermography and Reliability, H.H. Wills Physics Lab., University of  
Bristol, Tyndall Avenue, Bristol, BS8 1TL, United Kingdom

\*[bahar.oner@bristol.ac.uk](mailto:bahar.oner@bristol.ac.uk), [martin.kuball@bristol.ac.uk](mailto:martin.kuball@bristol.ac.uk)

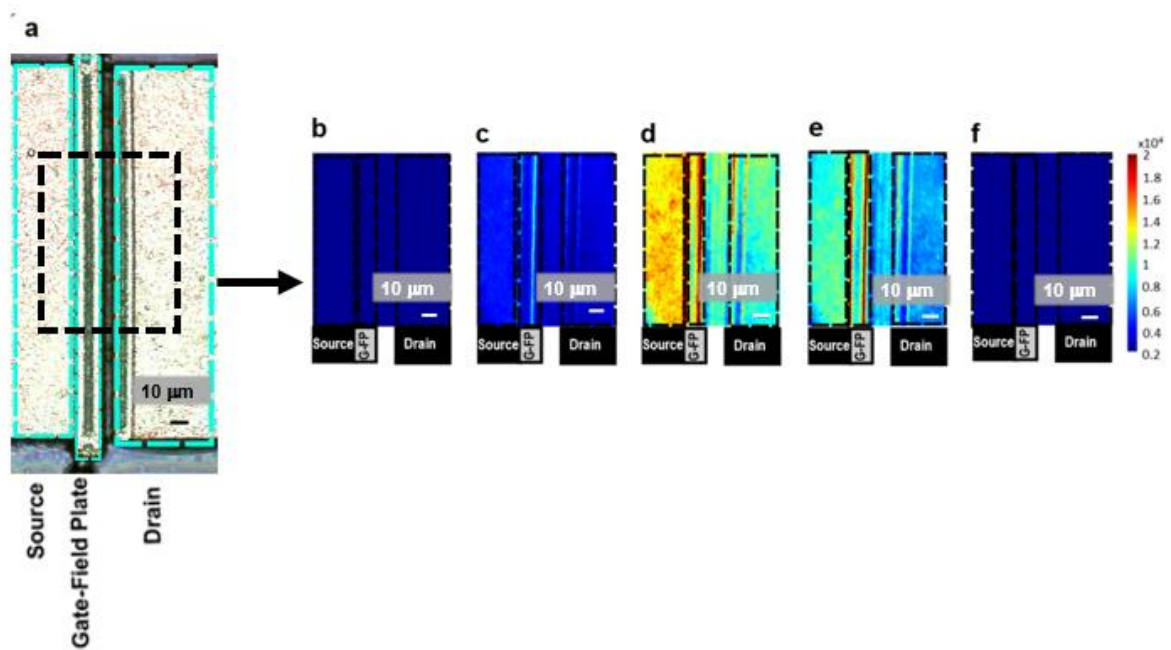


**Figure S1. Photoluminescence emission intensity of the QRs at different wavelengths, in the region of interest (ROI) deposited on the device under test (DUT), with the single-finger GaN on Si device in the ON state with  $V_{ds}=10$  V,  $I_{ds}=83.2$  mA,  $P_{diss}=4.165$  W/mm,  $T_{back\ plate}=25^{\circ}\text{C}$ .** (a) Optical image of a QR deposited test sample. The black dotted rectangle shows the ROI. Emission intensity of the monochrome images shown is at (b) 440 nm (c) 540 nm (d) 570 nm (peak QR emission intensity) (e) 600 nm (f) 720 nm recorded over a time interval of 1200 ms. Emission intensity maps show that the QR distribution is non-uniform over the ROI. However, this nonuniformity is not detrimental to the thermal image reconstruction if the signal to noise ratio remains above a threshold. Temperature values can be reconstructed at the all pixels in the ROI can having a peak emission intensity  $>350$  counts per pixel.

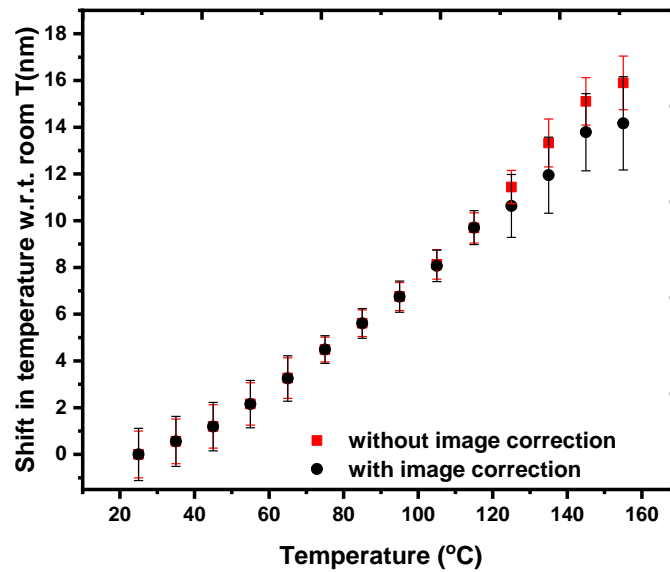


**Figure S2. Effect of x-y drift image correction on calibration.** x-y drift is more significant at higher temperature due to thermal expansion.

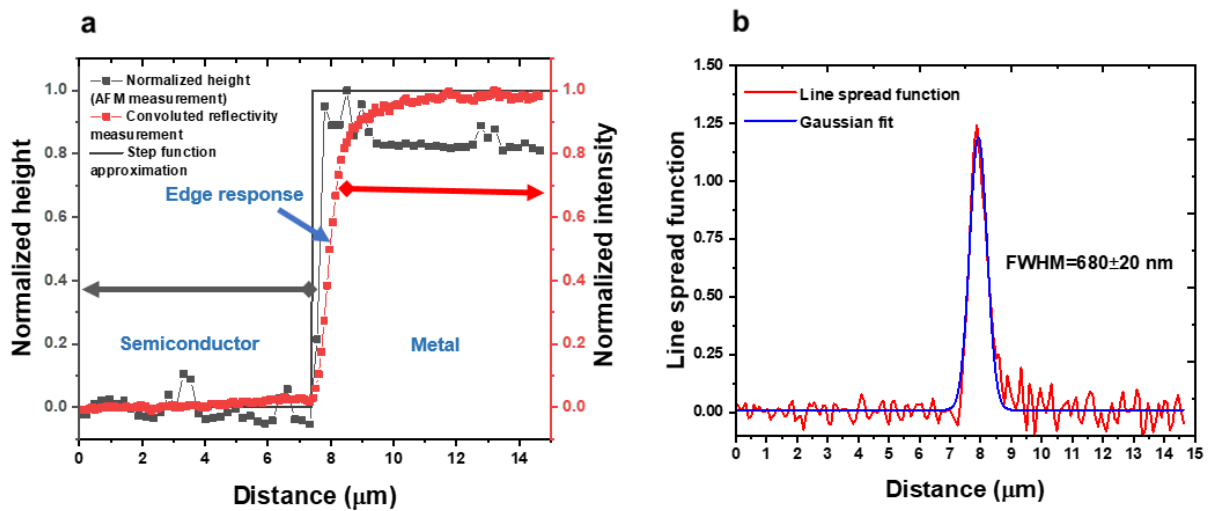


**Figure S3. (a)** Measured white light intensity reflected from the sample (tunable filter set to 560 nm) and the normalized height profile of the knife edge structure determined by AFM, edge response showing the image blur due to the spread function. AFM scan shows that the knife edge can be approximated as a step function for simplicity (The knife edge structure is similar to a step function with an R-square of 0.924 ) **(b)** The differentiation of the

convoluted image intensity shown in (a) gives the line spread function (LSF) of the imaging system.

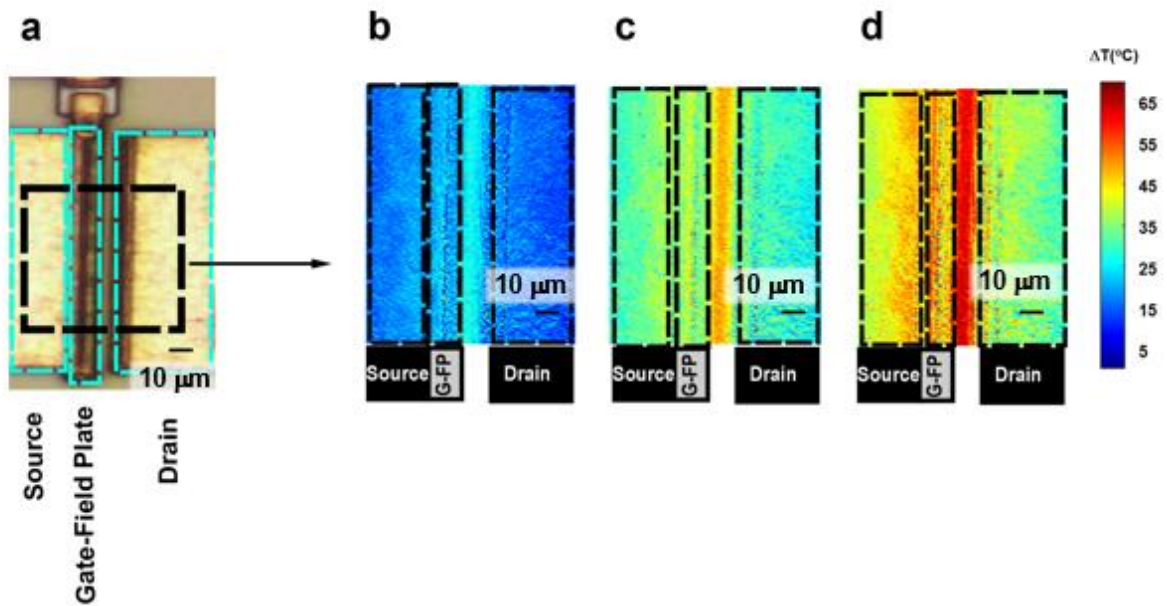


**Figure S4. HQTl determined temperature rise for different device power dissipation in the device center region at  $T_{\text{back plate}}=25^{\circ}\text{C}$ .** (a) Optical image of the DUT. Black dotted rectangle shows the ROI. Temperature maps of the ROI at (b)  $V_{\text{ds}}=5\text{ V}$ ,  $I_{\text{ds}}=62.5\text{ mA}$ ,  $P_{\text{diss}}=1.56\text{ W/mm}$  (c)  $V_{\text{ds}}=8\text{ V}$ ,  $I_{\text{ds}}=78.6\text{ mA}$ ,  $P_{\text{diss}}=3.145\text{ W/mm}$  (d)  $V_{\text{ds}}=10\text{ V}$ ,  $I_{\text{ds}}=83.2\text{ mA}$ ,  $P_{\text{diss}}=4.165\text{ W/mm}$ .

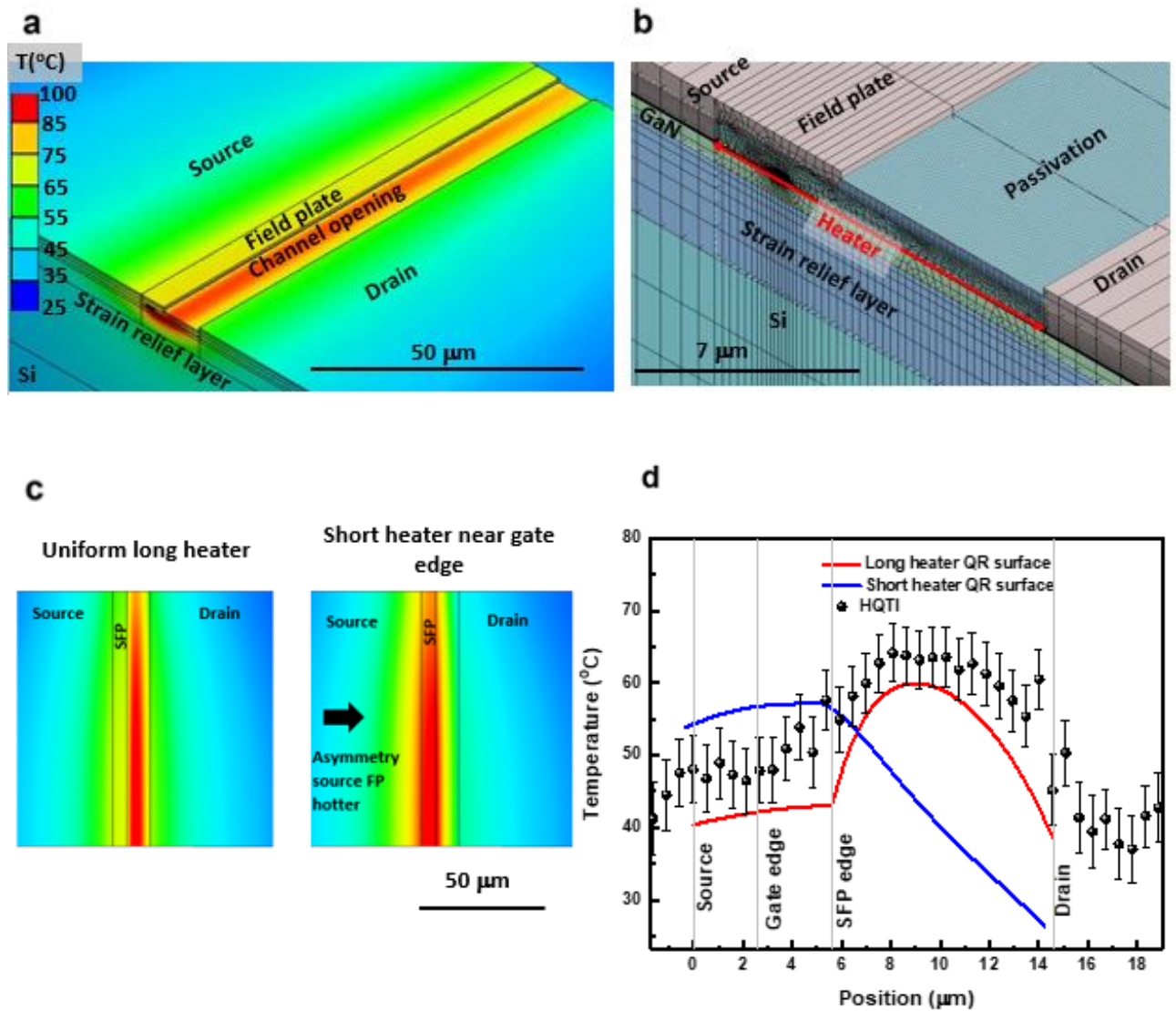


**Figure S5. Thermal FEM model of the  $\frac{1}{2}$  of the device, simulated at  $P_{\text{diss}}=4.165\ \text{W}/\text{mm}$ .**

(a) Overview of the FEM model, showing the epitaxial layers. (b) Mesh distribution and the heater input between the source and the drain contacts. The meshing was refined until the thermal error decreased to  $\sim 10^{-5}\ \text{W}/\text{m}^2$ . (c) Thermal FEM showing the effect of heat source distribution on the temperature map of the source and FP metal. (d) FEM simulated surface temperature profile for long (uniform between the source and the drain) vs. short heater (concentrated near gate -  $0.5\ \mu\text{m}$  long) scenarios in order to evaluate the heater size assumption.

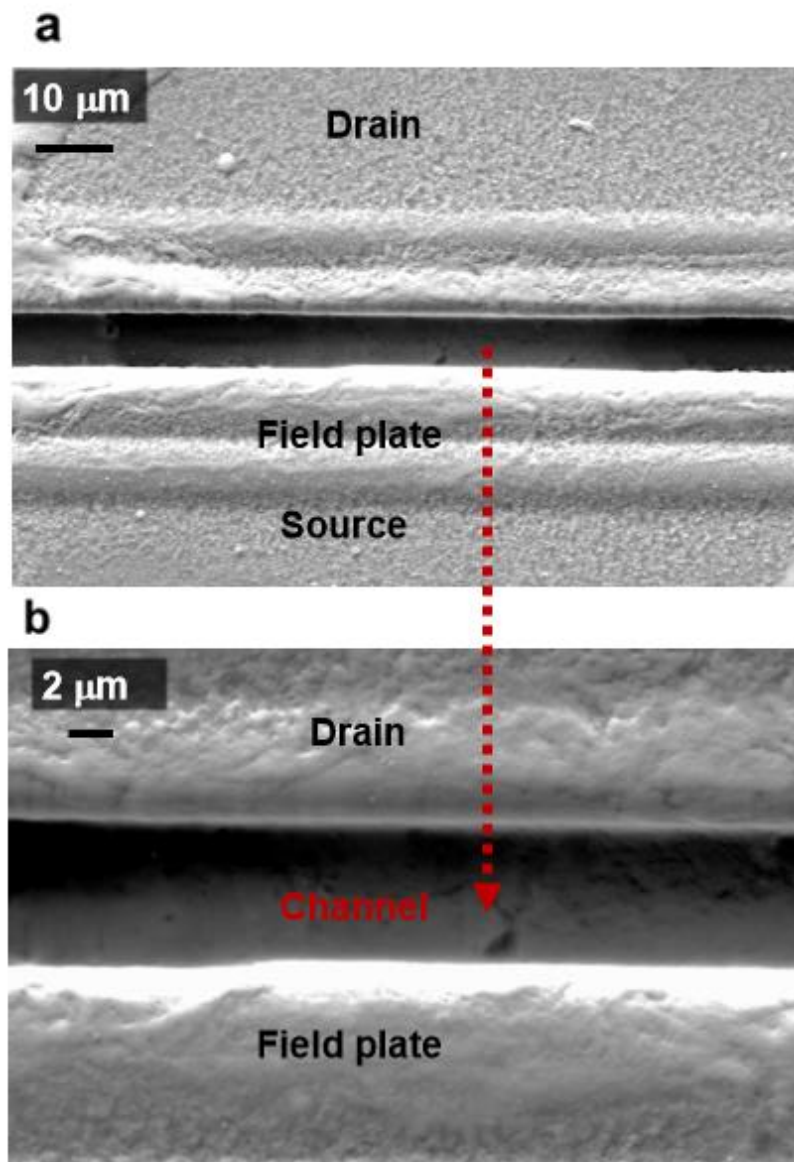


**Figure S6. SEM image of the QRs drop cast onto a DUT. (a)** SEM image showing that QRs form a layer-like distribution in the channel. **(b)** Magnified SEM image of the channel, showing that there is no apparent irregular clustering in the channel, while the image resolution is insufficient to observe single QRs.

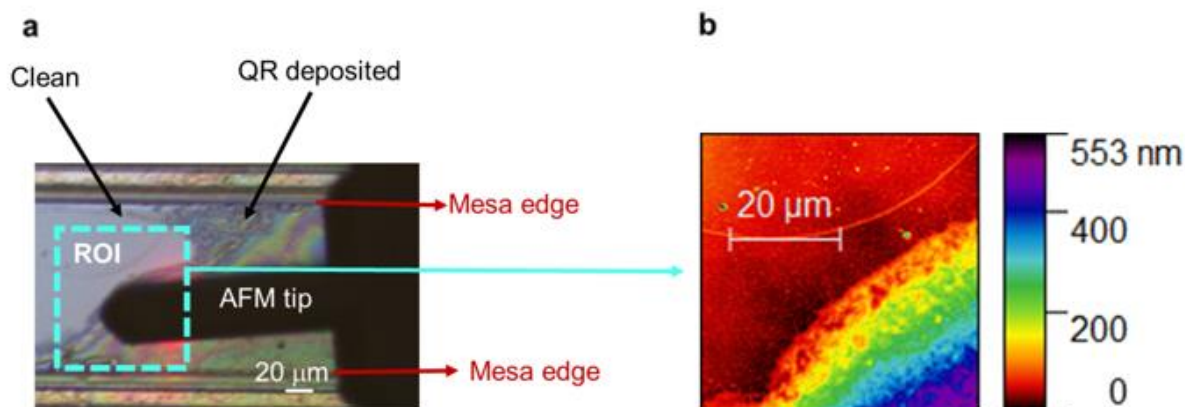


**Figure S7. AFM thickness measurements of the deposited QR layer at the intersection of the clean and deposited area to extract the upper limit of the QR deposited layer thickness. (a)** Region of interest (ROI) is a flat region between two adjacent cells, divided by the mesa edges, on the wafer. The ROI contains a region coated with QRs and a clean reference region for comparison. **(b)** Thickness profile of the ROI, at the edge of the deposited QR layer. The upper limit is  $\sim 500$  nm.

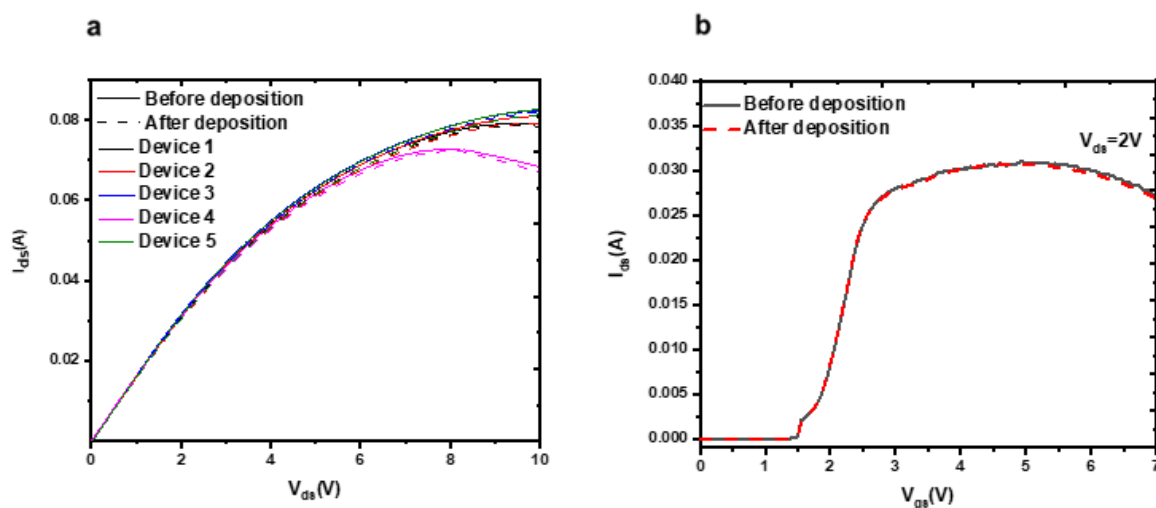


**Figure S8. Device characteristics measured before and the after the QR deposition. (a)** IV curve of passivated, GaN-on-Si devices measured at  $V_{gs}=5V$ , before and after QR deposition. Five devices were measured to verify the repeatability and consistency of the

results. (b) Transfer characteristics, before and after QR reposition, showing the threshold voltage does not change after the deposition.

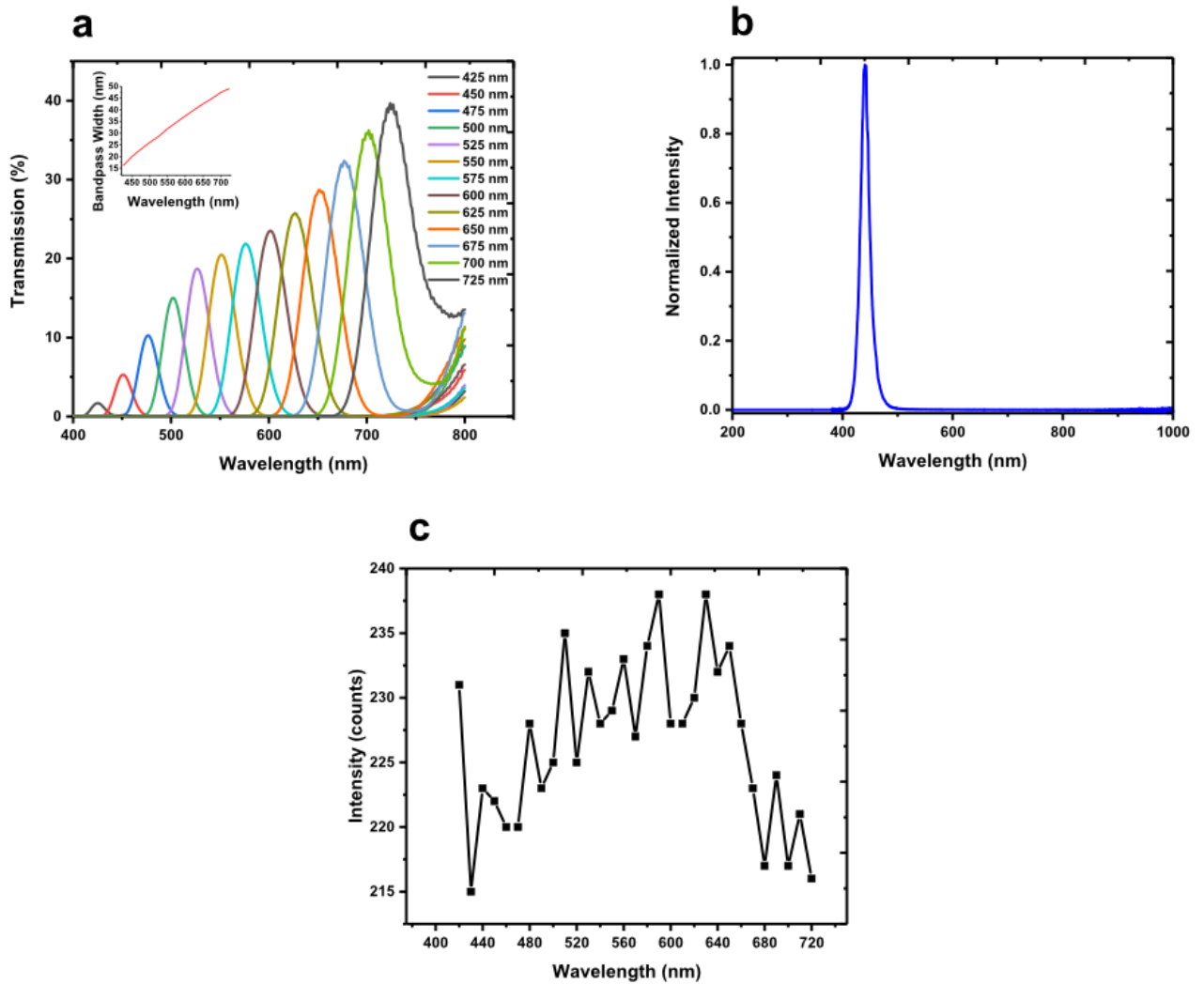


**Figure S9. Optical transmission properties of the components of system built. (a)** Tunable filter transmission response (Thorlabs KURIOS-VB1/M 420-730 nm, wide setting). **(b)** Blue LED emission spectrum (Thorlabs M450LP1). **(c)** Spectrum recorded from the DUT without QRs deposited with integration time of 1200 ms, i.e., the background signal.

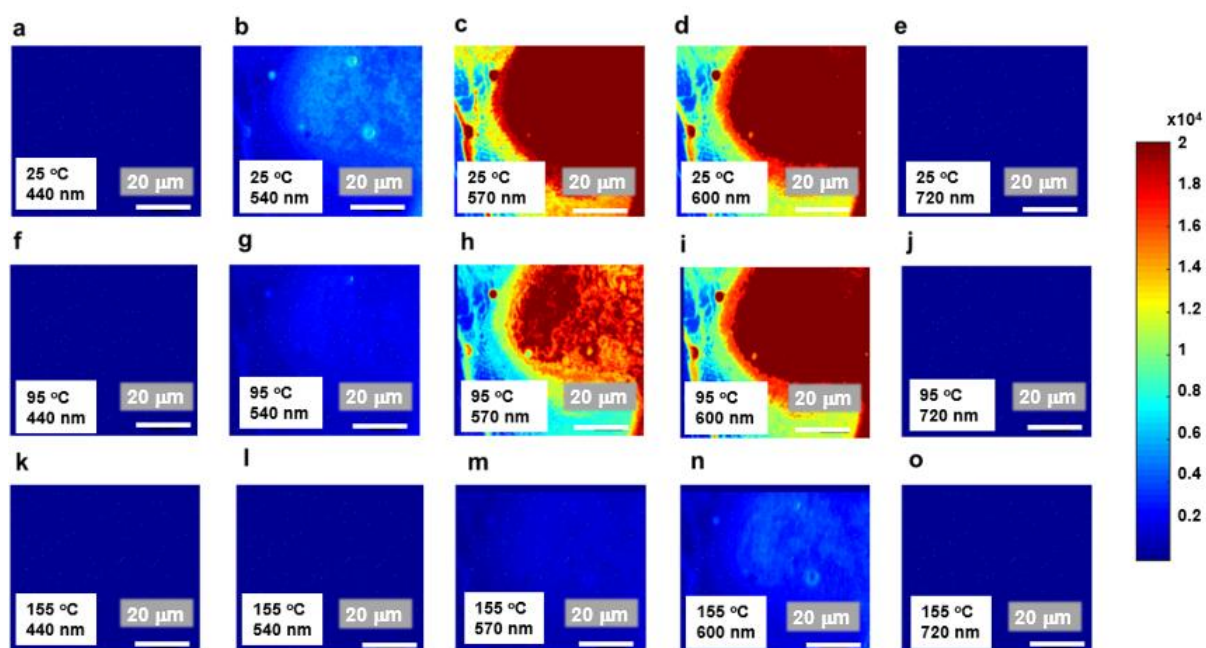


**Figure S10. QR photoluminescence emission intensity images of the Si calibration sample after deposition of the QRs, integrated of a time of 8 s, illustrating quenching of QRs with increasing temperature. (a-e) 440 nm-720 nm at 25 °C; (f-j) 440 nm-720 nm at 95 °C ; (k-o) 440 nm-720 nm at 155 °C.**

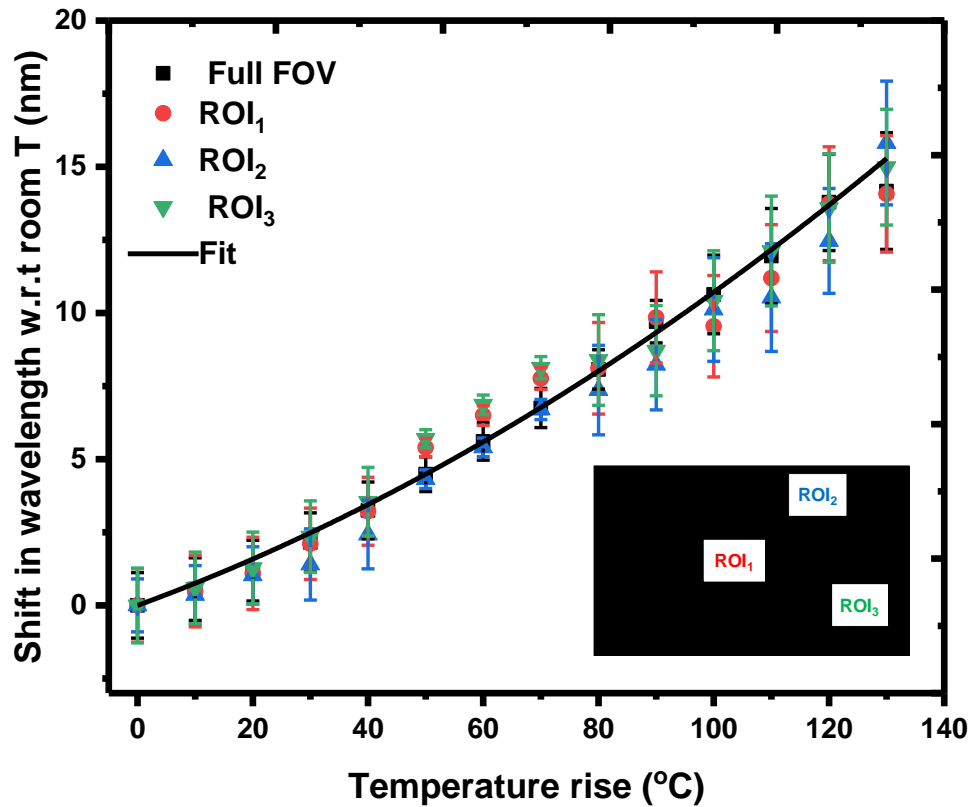


**Figure S11. Temperature induced shift in photoluminescence QR peak position, for three different locations on a Si wafer with QR deposited upon, together with fit obtained from averaging over the full field of view (FOV). The R-square value calculated for the 2<sup>nd</sup> order polynomial fits at each ROI is larger than 0.97 illustrating that averaging over the FOV for calibration is a valid approach.**

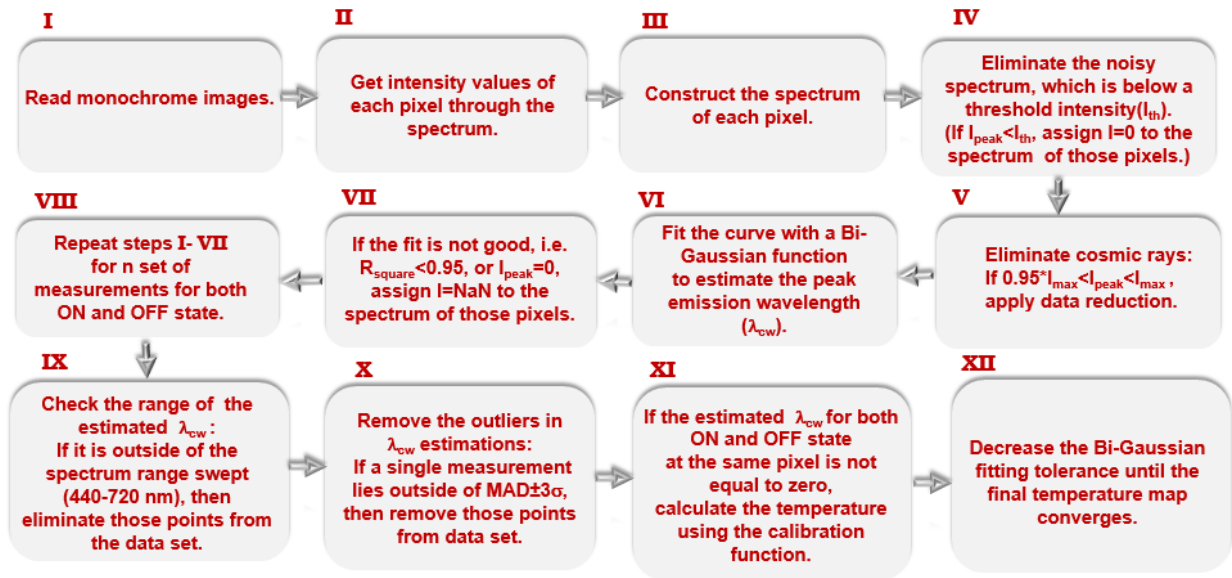


**Figure S12. Flow chart of the image processing algorithm.**

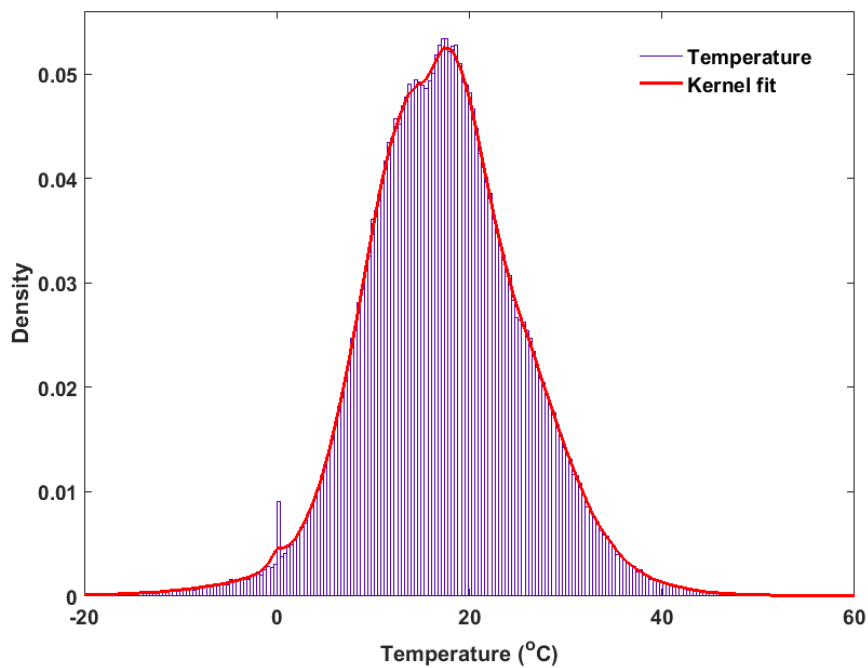


**Figure S13. Distribution of HQTl mean temperature recorded over the device in the pinched-OFF state at a base plate temperature of 25°C. The histogram was fitted to Kernel. The population mean of the mean temperature distribution across the 520x696 pixel image size is ~20 °C and the standard deviation is ~8 °C, showing that the estimation covers the actual channel temperature.**

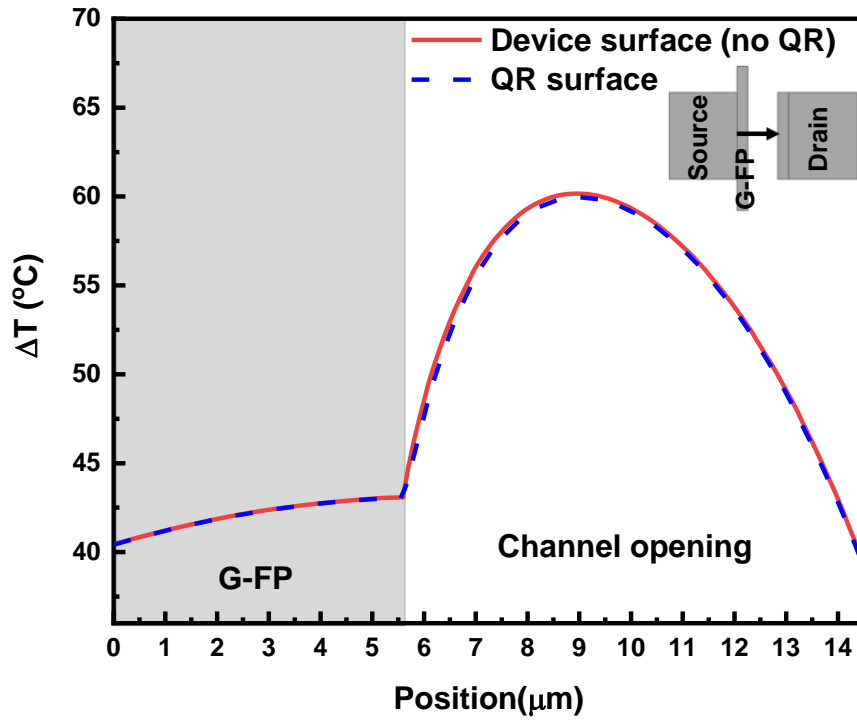


**Figure S14. Effect of QR deposition layer on temperature at the device top surface with the device operated at  $P_{\text{diss}}=4.165$  W/mm.** A thermal conductivity of 4.9 W/mK was considered for the QR layer of 500 nm. The simulations show that QR layer modifies the device surface temperature by only  $\sim 0.1^\circ\text{C}$ .

## Error analysis

As the uncertainty includes both the systematic errors and the random errors, we analysed these two contributions separately. Fig. 5b shows that there is no temperature offset at zero power dissipation, i.e.  $\Delta T$  is zero as expected, indicating that the systematic errors are negligible compared to the random errors. Other sources of uncertainty, other than random statistical errors, include errors in the fitting function coefficients. To estimate its effect on the temperature measurements, for a representative example, the deviation of the mean temperature estimations was obtained by applying the upper and lower limits of the calibration function, resulting in  $\pm 7$  °C for a sample size of  $n=3$  measurements for the DUT presented here for absolute device surface temperature of  $\sim 90$  °C, by calculating the difference between the maximum and minimum estimated mean temperature in the channel opening at each pixel. This value is within the precision of the measurement for  $n=3$  sample ( $\sim 7$  °C), indicating that the error contribution from calibration function fitting is small. We concluded that the systematic errors are small in our system at the measurement conditions when compared to the random errors. The error bars reported in this work are defined as the statistical random error, which also corresponds to the precision of the measurement.

Increasing the number of successive measurements ( $n$ ) increases the precision by  $1/\sqrt{n}$  because the precision of temperature estimation at a particular pixel is defined as the standard deviation of the population mean temperature at that pixel, divided by the square root of the number of measurements, i.e.  $\sigma/\sqrt{n}$ , which corresponds to the standard deviation of the “sample” mean from the “population” mean . The temperature estimations reported in this work represent this sample mean over 7 successive measurements and the error associated with this indicates the deviation of the sample mean from the population mean.

In order to estimate the accuracy of the mean temperature calculation, a Kernel distribution (non-parametric distribution) shown in Sup. Fig. 13 was fitted to the histogram using MATLAB Distribution Fitting application and a mean temperature of  $\sim 20$  °C with a standard deviation ( $\sigma$ ) of 8 °C was obtained. As this analysis was performed for a sufficiently large number of pixels, i.e. a 520x696 pixel image, with a non-Gaussian distribution, we consider the estimated mean as the “population” mean, rather than the “sample” mean, i.e., the population representing all the pixels of the image where the image processing performed. Therefore, we report here the standard deviation rather than the standard error of the mean for this analysis.